

Article

The Origins of the High Performance of Pd Catalysts Supported on Carbon Black-Embedded Carbon Nanofiber for Formic Acid Oxidation

Norraihanah Mohamed Aslam ¹, Takuya Tsujiguchi ^{2,*}, Yugo Osaka ² and Akio Kodama ²

¹ Division of Mechanical Engineering, Graduate School of Natural Science and Technology, Kanazawa University, Kakumamachi, Kanazawa, Ishikawa 920-1192, Japan; norraihanah.m.a@gmail.com

² Faculty of Mechanical Engineering, Institute of Science and Engineering, Kanazawa University, Kakumamachi, Kanazawa, Ishikawa 920-1192, Japan; y-osaka@se.kanazawa-u.ac.jp (Y.O.); akodama@se.kanazawa-u.ac.jp (A.K.)

* Correspondence: tsujiguchi@se.kanazawa-u.ac.jp; Tel.: +80-76-264-6473

Received: 12 November 2019; Accepted: 13 December 2019; Published: 16 December 2019



Abstract: In this study, we developed a carbon black (CB)-embedded carbon nanofiber (CNF) as a Pd support, which showed a high level of formic acid oxidation reaction (FAOR) activity. For the support preparation, heat treatment involving calcination at 1000 °C in a nitrogen atmosphere (carbonization) followed by calcination at 850 °C in water vapor (steam activation) was conducted to form a CB, which contained carbon nanofibers made from a polyacrylonitrile (PAN) fiber prepared by electrospinning. This catalyst showed a high level of FAOR activity. In this situation, the CB was also heat-treated, therefore, it was unclear whether the origin of the high FAOR activity of the CB-embedded CNF was caused by the CNF itself or the heat treatment of the CB. In order to establish the cause of the high FAOR activity of the CB-embedded CNF, the CBs underwent several heat treatments; i.e., stabilization, carbonization, and steam activation. Two types of carbon black with different pore structures, i.e., Ketjen black and Vulcan XC-72, were used to investigate the FAOR activity. The appropriate heat treatment of the CB promotes the improved FAOR activity; however, excessive heat treatment caused a deterioration in the FAOR activity, especially for Ketjen due to the presence of numerous micropores. However, by embedding the CB into the CNF, the FAOR activity improved, especially in the case of Ketjen, even though the embedded CB underwent several heat treatments. The optimum ratio of CB/PAN in the CB-embedded CNF was also investigated. The highest FAOR activity was observed at 0.25 CB/PAN for both the Vulcan and Ketjen. The electronic state of Pd3d in which the binding energy of the metallic Pd shifted to a lower binding energy suggested that the metal–support interaction is strong at the CB/PAN ratio of 0.25. On the basis of these results, it was found that heat treatment of the CB by embedding it in the CNF is a promising way to achieve a metal–support interaction without destroying its structure.

Keywords: formic acid oxidation reaction; embedded CNF; heat treatment; morphology; pore distribution

1. Introduction

Direct formic acid fuel cells (DFAFCs) are a promising type of direct liquid fuel cell due to their favorable oxidation kinetics which enable low temperature operation (50–80 °C), a high theoretical open-circuit voltage (1.45 V), and a relatively low fuel crossover through the Nafion membrane [1,2]. Platinum (Pt) and palladium (Pd) have been widely studied as anode catalysts for DFAFCs because of their interactions with formic acid, in which Pd tends to break the O–H bonds across the entire potential window, and Pt discriminates between the cleavage of O–H bonds at a high overpotential

and the cleavage of C–O and/or C–H at a low overpotential [1,3–5]. The difference between the reaction pathways for formic acid oxidation on the Pt and Pd catalysts was pointed out by Jayashree et al. [6]; it was also experimentally confirmed that no CO build-up occurred and a higher current density was achieved for formic acid oxidation on Pd [5]. In fact, DFAFCs exhibiting high power densities were reported when Pd- or Pd-based catalysts were used as the anode catalysts [7].

It has been reported that supported catalysts with a high surface area, good electrical conductivity, good electrochemical stability, and suitable porosity exhibit a good stability and higher activity than unsupported catalysts [8–12]. Catalyst support materials have been roughly classified as carbon-based supports and non-carbon-based supports [9]. Non-carbon-based supports, such as titania [13–15], indium oxide, alumina, silica [13], ceria [15], zirconia, tungsten oxide, and conducting polymers [9], can improve reaction kinetics due to metal–support interactions; however, their electrical conductivity is lower than that of carbon. The electrical conductivity increases when non-carbon materials are embedded with carbon nanofibers (CNFs) as the catalyst support, as pointed out by Ito et al. [14] and Kunitomo et al. [15]. In their studies, the PtRu catalyst on non-carbon supports, such as ceria particles [15] and titania particles [14], gave lower performances for methanol oxidation compared to the carbon-based supports. By embedding the non-carbon material into the CNFs, metal–support interactions were obtained as a result of the high electrical conductivity of the CNFs. In our previous studies, we also demonstrated that Pd supported by TiO₂, SiO₂, and carbon black (CB) (Vulcan) embedded into the CNFs showed higher formic acid oxidation reaction (FAOR) activities than unembedded CNFs [13]. The high FAOR activity of the TiO₂- and SiO₂-embedded CNFs results from the metal–support interactions with a high electrical conductivity similar to the case in Ito’s study [14] and Kunitomo’s study [15]. On the other hand, in the case of Vulcan XC-72, which has a high electrical conductivity but no or fewer metal–support interactions, it is considered that the metal–support effect becomes significant or the CB properties (such as the surface area or pore volume) change through the heat treatment of CB, as the CB-embedded CNF is prepared over several heat treatment steps, namely, stabilization, carbonization, and steam activation.

There are several reports related to the effect of the heat treatment of CB on its properties and electrochemical reaction. An enhancement of the surface area caused by heat treatment has been reported by Holade et al. for Vulcan XC-72 and Ketjen black. They revealed that a significant enhancement of the surface area through heat treatment (carbonization) concomitantly occurred with an improvement in the catalytic activity by increasing the specific electrochemical surface area (ECSA) [11]. Inoue et al. also proposed that heat treatment of CB affects oxygen reduction reaction (ORR) activity of the Pt surfaces [16]. Heat treatment of the carbon-based supports improved the electrocatalytic activity and stability of the ORR catalysts [17–19]. Thus, there are several reports in which the heat treatment of CB contributes to an enhanced ORR activity, Brunauer-Emmett-Teller (BET) surface area, and stability; however, whether or not heat treatment of CB is also effective for improving the FAOR activity requires further investigation. Moreover, to the best of our knowledge, there is no study in which steam activation was selected as a heat treatment for CB. By undergoing the heat treatment of CB-embedded CNF contributed to FAOR improvement, morphology, and pore structure; the various heat treatments for carbonization, steam activation, and both heat treatments of CB were investigated in this study. Carbonization and steam activation, which were conducted to prepare the CB-embedded CNF in a previous study [13], were selected as the heat treatments to clarify the factors governing the performance enhancement of the CB catalyst supports. Vulcan XC-72 and Ketjen black were selected as the CBs because they are widely used as catalyst supports but have different pore structures. Different weights of the CB-embedded CNFs for Vulcan XC-72 and Ketjen black were also synthesized to compare the effect of the heat treatment of CB, and the quantity of CB in the CNF was studied to find the optimum weight ratio of CB in the CNF.

2. Experimental

2.1. Catalyst Preparation

Commercial Vulcan XC-72R (Cabot Corp., MA, USA) and Ketjen black (Lion Speciality Chemicals Co. Ltd., Tokyo, Japan) were used for the Pd support and were embedded into the CNFs. Vulcan embedded into the CNFs (VECNF) and Ketjen embedded into the CNFs (KECNF) were prepared using the following procedure. Polyacrylonitrile (PAN, Sigma-Aldrich Co., Ltd., MO, USA) was used as the carbon source for the nanofibers. Solutions containing PAN and CB were individually prepared by dissolving PAN and CB into dimethylformamide (DMF, Wako Pure Chemicals Ind., Ltd., Osaka, Japan) using a planetary centrifugal mixer (ARE-310, THINKY Corp., CA, USA) for 10 min for each solution. The CB/DMF solution was added to the PAN/DMF solution and mixed for 5 min in a planetary centrifugal mixer. The weight ratio of CB to PAN was varied between 0 and 0.5. The mixture of CB and PAN was transferred to a glass syringe equipped with a stainless steel needle for electrospinning at 0.05 mL min^{-1} in an electric field through a syringe pump (AS One Co., Ltd., Osaka, Japan) to control the solution feed rate of the ink. Electrospinning was conducted by applying an 18 kV potential difference between the needle and the rotating collector using a high-voltage power supply (Element Co., Ltd., Tokyo, Japan). The collector was covered with aluminum foil and placed at a distance of 20 cm from the needle. After the polymer nanofibers were obtained from the electrospinning process, they were stabilized in a tube furnace at $250 \text{ }^\circ\text{C}$ in an air atmosphere for 10 h. After stabilization, the nanofibers were calcined at $1000 \text{ }^\circ\text{C}$ in a nitrogen atmosphere for one hour (carbonization process). Finally, steam activation was conducted at $850 \text{ }^\circ\text{C}$ for one hour in a humidified nitrogen flow with a $70 \text{ }^\circ\text{C}$ dew point. To check the effect of the heat treatment on the Vulcan (C_v) and Ketjen (C_k), several CB samples were also prepared with different heat treatments. After stabilization, one set of CB samples was carbonized at $1000 \text{ }^\circ\text{C}$ in flowing nitrogen, and the samples were denoted as C_v -carb or C_k -carb. Another set of CB samples was subjected to steam activation at $850 \text{ }^\circ\text{C}$ in flowing humidified nitrogen with a $70 \text{ }^\circ\text{C}$ dew point, and these samples were denoted as C_v -act or C_k -act. A final set of CB samples was heat-treated in a similar manner to the VECNF and KECNF samples and was denoted as C_v -all or C_k -all. As a reference, CBs without heat treatment were also used as catalyst supports and these samples were denoted as C_v -no and C_k -no.

A 20 wt.% quantity of Pd was deposited on each of the supports by chemical reduction using NaBH_4 (Wako Pure Chemicals Ind., Ltd.) and PdCl_2 (Wako Pure Chemicals Ind., Ltd.) as the precursors. After the heat treatment process, the supports were ultrasonically dispersed in distilled water for 30 min. The precursor was added to this solution while stirring, then heated to $80 \text{ }^\circ\text{C}$ for 1 h. The pH of the solution was maintained at 8–9 by adding NaOH. A 0.2 M NaBH_4 solution was then added dropwise. The solution was stirred for a further 1 h, then cooled before drying and washing with distilled water. The catalyst was finally dried for 3 h at $120 \text{ }^\circ\text{C}$. The catalysts were denoted as Pd/ C_v , Pd/ C_k , Pd/VECNF, and Pd/KECNF, respectively. For VECNF and KECNF, the CB/PAN ratio was also indicated after the sample name; for example, Pd/VECNF [0.5] denotes the 0.5 CB/PAN ratio and [0.0] denotes CNFs without CB (Pd/CNF).

2.2. Material Characterization

The surface morphologies of the synthesized catalysts were investigated using a field emission scanning electron microscope (FESEM; JSM-7500F, JEOL). The crystal structures of the prepared catalysts were determined from the X-ray diffraction (XRD) patterns of the powder samples using an X-ray diffractometer (MiniFlex, Rigaku). The source of the X-rays was Cu-K α , operating at 2.7 kV and 30 mA. The crystallite size, d , of the Pd was calculated from the width at half height of the diffraction peak arising from the Pd crystals at 40° using Scherrer's equation, $d = 0.9\lambda / \beta \cos\theta$, where λ is the wavelength of the X-rays (1.54056 \AA), θ is the angle at the peak, and β is the width of the peak at half height.

Nitrogen adsorption–desorption isotherms were measured at 77 K using a BELSORP MAX (MicrotracBEL Corp., Osaka, Japan) to reveal the pore structure of the catalysts. Pd catalysts deposited on the supports were degassed at 200 °C for 10 h prior to the measurements. The BET surface area and total pore volume were calculated in the relative pressure interval of 0.0 to 0.5 using the Brunauer–Emmet–Teller (BET) method. The pore volumes of micro (>2 nm) and meso (2–50 nm) were obtained using the microporous (MP) method and Barrett–Joyner–Halenda (BJH) method, respectively. The macropore volume was obtained by subtracting the micro- and mesopore volumes from the total pore volume obtained by the BET method.

X-ray photoelectron spectroscopy (XPS) was recorded using a JEOL JPS-9010 photoelectron spectrometer with an Mg K α X-ray source to determine the surface properties of the catalyst. Narrow photoelectron scans were recorded of the Pd3d regions and the binding energies were corrected based on the C_{1s} peak. After Shirley background removal, the peaks were fitted by SpecSurf V1.9.3.2 (JEOL Ltd., Tokyo, Japan) using Gaussian–Lorentzian functions.

2.3. Electrochemical Measurements

The FAOR activity of the catalysts was measured by cyclic voltammetry (CV) and ECSA using a three-electrode cell with a Pt wire as the counter electrode, mercury–mercurous sulfate as the reference electrode, and a fixed 3 mm in diameter glassy carbon electrode (GCE) as the working electrode. The catalyst ink was prepared by mixing 5 mg of the catalyst in a solution of 160 μ L distilled water and 160 μ L acetone with 25 μ L of a 5 wt.% Nafion solution (Wako Pure Chemicals Ind., Ltd.). The mixture was then dispersed by ultrasonication for 30 min, and 2.5 μ L of the resultant catalyst ink was deposited onto the glassy carbon electrode and dried at room temperature for 10–15 min. The catalyst loading was estimated to 0.52 mg_{catalyst} cm^{−2} in each catalyst, hence, the loadings of each electrode for all catalysts were estimated to 0.10 \pm 0.01 mg_{Pd} cm^{−2}. In order to avoid the effect of catalyst loading on the electrode on the CV results, the results were normalized by mass activity (mA mg_{Pd}^{−1}). The electrode was finally dried at 80 °C for one hour. A mixture of 3 M formic acid containing 0.5 M sulfuric acid was used as the electrolyte for the CV measurements during the FAOR activity evaluation. ECSA was also calculated by CV measurement using only 0.5 M sulfuric acid. Both methods were started with nitrogen bubbling for 30 min to remove the oxygen from the electrolyte. ECSA was calculated to measure the active site of the Pd catalyst that is attributed to the optimum utilization of the Pd catalyst during the electrochemical reaction. An ECSA measurement was carried out under similar operating conditions and evaluated using a similar setup to the CV. The ECSA values were calculated by the equation, ECSA = Q/q₀, where Q is the electric charge calculated from under the graph area at a room temperature of 26 °C in saturated nitrogen of a 0.5 M sulfuric acid solution and the q₀ is 420 μ C cm^{−2} [20].

3. Results and Discussion

3.1. Effect of Heat Treatment of Carbon Black Supports on the Properties of Pd/C Catalysts

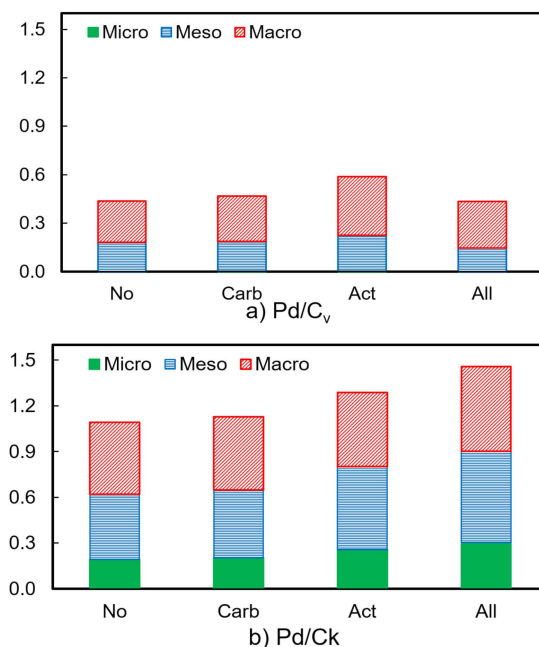
The prepared Pd catalysts supported by the heat-treated carbon blacks (Pd/C_v and Pd/C_k) were characterized. Table 1 summarizes the BET surface area, pore volume based on the MP and BJH analyses, and crystallite size of the Pd catalysts determined by XRD. It can be seen from Table 1 that the BET surface area of the Pd/C catalysts increased when Pd was deposited onto heat-treated carbon support, irrespective of the kind of heat treatment and CB. This means that the BET surface area was increased by the heat treatment, which is consistent with the phenomena reported in the literature [11,21]. Both the Pd/C_k and Pd/C_v that went through both carbonization and steam activation have the highest BET surface areas. This is due to the more porous construction caused by steam activation [22] which leads to a higher BET surface area. The BET surface areas of Ketjen and Vulcan proportionally increased with the intensity of the heat treatment, i.e., No < Carb < Act < All, due to the development of the micropore structure of the CBs.

Table 1. Summary of the Brunauer-Emmett-Teller (BET) surface areas, pore volumes, and Pd crystallite sizes of the prepared Pd/CB catalysts.

| Heat Treatment on Carbon Support | BET Surface Area ($\text{m}^2 \text{g}^{-1}$) | | Pore Volume ($\text{cm}^3 \text{g}^{-1}$) | | Pd Crystallite Size (nm) | |
|----------------------------------|---|-------------------|---|-------------------|--------------------------|-------------------|
| | Pd/C _v | Pd/C _k | Pd/C _v | Pd/C _k | Pd/C _v | Pd/C _k |
| No | 85 | 581 | 0.44 | 1.09 | 6.6 | 3.9 |
| Carbonization (Carb) | 166 | 609 | 0.47 | 1.13 | 7.7 | 4.4 |
| Steam activation (Act) | 221 | 714 | 0.59 | 1.29 | 9.4 | 2.2 |
| Carb and act (All) | 256 | 840 | 0.53 | 1.46 | 4.6 | 4.5 |

There is a big difference in the surface area between the Pd/C_ks and Pd/C_vs. This is due to the difference in the pore properties between the commercial Vulcan and Ketjen. Vulcan is a nonporous carbon material which has no or few micropores, and Ketjen is a porous carbon black which has a large fraction of micropores and broad pore size distribution [23]. Regarding the crystallite size of Pd, there is no particular trend in the heat treatment although Pd/C_k showed smaller crystallite sizes, i.e., 2.2–4.5 nm, than that of Pd/C_v, i.e., 4.6–9.4 nm. On the basis of these results, heat treatment provides an enhancement of the total surface area, which is a trend similar to previous studies [13].

Figure 1 and Figure S1 shows the pore volume distribution, while Figure S2 shows nitrogen adsorption and desorption isotherms for Pd/C with the different CBs and heat treatments. The pore volume was classified according to the pore size: macropore (>50 nm), mesopore (2–50 nm), and micropore (<2 nm) [11,17]. Generally, the total pore volumes of the Pd/C_ks were significantly higher than those of Pd/C_v irrespective of the heat treatment type. For the Vulcan, the volume of the mesopore for Pd/C_v-carb was similar to that of Pd/C_v-no. Moreover, the volume of the macropore Pd/C_v increased from Pd/C_v-no resulting in the increased total pore volume.

**Figure 1.** Pore volume distribution for Pd/C for different carbon blacks (CBs) and heat treatments for (a) Pd/C_v and (b) Pd/C_k.

On the basis of these results, it is suggested that the mesopores would grow into macropores, and the small pores, such as the micro- or small mesopores, would be produced by the carbonization process. Referring to the effect of the steam activation, the total pore volumes of the Pd/C_v-act were much higher than those of Pd/C_v-no and Pd/C_v-carb. During the steam activation process, oxygen contained

in the water molecules reacted with the surface carbon of the CB resulting in a greater pore production compared to the carbonization process, although the CB was calcined at a temperature lower than the carbonization process. In other words, the intensity of the heat treatment, which indicates the degree of the pore growth and pore production, was higher in the case of steam activation than carbonization. On the other hand, it was found that the total and mesopore volumes of Pd/C_v-all were the lowest among all the cases. This is due to the excessive growth of the pores that underwent two heat treatment processes. During the carbonization process, some of the mesopores grew and new small mesopores were produced. The newly produced small mesopores and the mesopores grown during the carbonization process were considered to have grown even more in the steam activation process. However, the macropore volume of Pd/C_v-all was lower than that of Pd/C_v-act. This fact indicated that the macropores disappeared when the excessive heat treatment was finished. It is known that macropores are formed by aggregates and/or agglomerates [23]. Therefore, it is considered that a part of the aggregates or agglomerates were possibly broken or separated into particles due to the excessive heat treatment, resulting in the macropores disappearing. On the basis of these results, it can be concluded that the BET surface area increased after the heat treatment due to the development of a microporous structure; however, excess heat treatment, such as that used to prepare Pd/C_v-all, causes splitting of the aggregates or agglomerates.

However, for Pd/C_k, Pd/C_k-all demonstrated the highest pore volume for each type of pore size. Increasing of the macropores in Pd/C_k-all was due to pore growth of the smaller pores such as the micropores and mesopores. Mesopores in Pd/C_k-act and Pd/C_k-all were more prevalent than those in Pd/C_k-no and Pd/C_k-carb. The total pore volume increased after the heat treatment and the total pore volume of Pd/C_k-all was the highest among all the Pd/C_k, although the total pore volume of Pd/C_v-all was lower than that of Pd/C_v-act. This difference is due to the hollow structure of Ketjen, which leads to a highly developed pore structure even without heat treatment. During the heat treatment, not only micropore generation, but also pore growth simultaneously occurred. In the case of Vulcan, the effect of the pore growth on the pore distribution was limited because the pore volume was already low without heat treatment; hence the excess heat treatment caused a reduction in the pore volume. On the other hand, in the case of Ketjen, the effect of pore growth, which caused an increase in the pore volume, was significant because there were numerous pores before the heat treatment. Therefore, the total pore volume did not decrease when carbonization and steam activation were conducted as a result of pore growth and a decrease in the pore volume, as the splitting of the aggregates or agglomerates cancel each other out, resulting in the large pores remaining unchanged.

3.2. Effect of Heat Treatment of Carbon Blacks on Formic Acid Oxidation Reaction Activity

Figure S3 shows the effect of the heat treatment of CB on the FAOR activity of the catalysts. The figure shows only the anodic scan of the CV for Pd/C, which corresponds to the electro-oxidation of formic acid. The peak current density occurs between 0.44 and 0.84 V vs. normal hydrogen electrode (NHE). In the case of Vulcan, the heat-treated CB, especially Pd/C_v-carb and Pd/C_v-act, showed significantly higher FAOR activities than Pd/C_v-no, as shown in Figure S3a. It has been reported that heat treatment increases the BET surface area and the electrical conductivity of CB [9,24]. The presence of defects on the catalyst support surface is understood to enhance the hydrogen spillover. Moreover, it has also been reported that the heat-treated CB improved the hydrogen spillover due to the increasing of the surface area and pore volume of the support [21,25]. The hydrogen spillover occurs when hydrogen atoms tend to diffuse and migrate from the external surface into the inter-planar spacing through defect sites on the surface of the heat-treated catalyst support. The acceleration of the dehydrogenation during the FAOR on a Pd surface is affected by the hydrogen spillover [25]. The higher FAOR activity of the heat-treated Pd/C_v observed here is attributed to these findings. On the other hand, in the case of Pd/C_v-all, the FAOR activity was lower than those of Pd/C_v-carb and Pd/C_v-act, even though the BET surface area was higher. This was due to the excessive heat treatment. Micropores were significantly developed by the heat treatment. Park et al. reported that Pt particles

were observed in the interior of the CB in which the microstructure developed, resulting in a decreased effective surface area of the Pt [26]. As a result of the excessive heat treatment, the micropore structure was excessively developed, resulting in a reduction in the effective surface area of Pd in the case of Pd/C_v-all. Moreover, there is the possibility that the splitting of the aggregates or agglomerates affects the FAOR activity since the electrical conductivity would be changed due to less contact between the primary carbon particles. These results suggest that there is an appropriate intensity of heat treatment to maximize the FAOR activity for the CB supports. The effect of the heat treatment of Pd/C_v on the ECSA of each catalyst is explained in the latter part of the paper.

In the case of Ketjen, the heat treatment did not improve the FAOR activity, despite an increase in the BET surface area. This is due to the pore structure of Ketjen, which has numerous pores and an initially high BET surface area compared to the Vulcan even without heat treatment. Similar to the case of Pd/C_v-all, the excessive development of a structure with small pores during heat treatment caused a decrease in the FAOR activity. Therefore, it was found that the heat treatment of the porous carbon, such as Ketjen, was not effective at enhancing the FAOR activity even though the BET surface area increased. Since both heat treatments for carbonization and steam activation result in a degraded Pd/C_k and Pd/C_v catalytic activity of the FAOR, it can be concluded that excessive heat treatment of the catalyst-supported CB caused deterioration of the CB structure. Hence, both heat treatments are only appropriate for the CB-embedded CNF. Table 2 summarizes the maximum mass activity of the FAOR and ECSA for Pd/C with various heat treatments. The calculated ECSA value for Pd/C_k was generally lower than that of Pd/C_v except for Pd/C_k-no. In the case of Pd/C_v, the heat-treated catalysts provided higher ECSA values compared to those of the untreated catalyst, indicating that the heat treatment contributes to enhancing the active site of the Pd/C catalyst. However, Pd/C_k-no showed a different behavior in which Pd/C_k-no obtained the highest ECSA at 17.0 m² g_{Pd}⁻¹ compared to the treated catalysts of Pd/C_k. The higher ECSA value indicates more available active sites since ECSA is one of the significant indicators of electrocatalyst performance [27]. This means that in the further heat-treated Pd/C_k, either the active sites were hidden inside the micropores and/or mesopores, or the connectivity of the ionomer decreased due to the broken pores compared to that which underwent no heat treatment.

Table 2. Summary of catalytic activity and electrochemical active surface area of Pd/C_v and Pd/C_k with various heat treatments.

| Catalyst | Mass Activity at E _p , i _{p-FAOR} (mA mg _{Pd} ⁻¹) | Peak Potential, E _p (V vs. normal hydrogen electrode, NHE) | Electrochemical Active Surface Area (m ² g _{Pd} ⁻¹) |
|-------------------------|---|--|--|
| Pd C _v -carb | 1397 | 0.76 | 22.9 |
| Pd C _v -act | 1667 | 0.84 | 26.1 |
| Pd C _v -all | 810 | 0.66 | 11.1 |
| Pd C _v -no | 250 | 0.44 | 7.1 |
| Pd C _k -carb | 1083 | 0.70 | 10.3 |
| Pd C _k -act | 845 | 0.64 | 8.8 |
| Pd C _k -all | 653 | 0.50 | 6.7 |
| Pd C _k -no | 1212 | 0.64 | 17.0 |

3.3. Characterization of Pd/CB Embedded in Carbon Nanofibers with Different Carbon Black Contents

Heat treatment, carbonization, and steam activation were conducted using CBs embedded in polymer fibers prepared by electrospinning (since this is required to carbonize them). Figure 2 shows the morphology of Pd/CNF, Pd/VECNFs, and Pd/KECNFs at different ratios of CB/PAN. The Pd particles were homogeneously dispersed along the CB-embedded CNF with the loading of Pd between 18–22 wt.%. The increasing ratio of CB/PAN distinctly showed changes in the decorated fibers with the existence of an increased coarse structure. There is an insignificant difference in the morphologies for both Pd/KECNF and Pd/VECNF at a low ratio: 0.125 for CB/PAN compared to the Pd embedded only in CNF. The roughness of the fiber surface increased in the case of Pd/KECNF [0.25] and Pd/VECNF [0.25], suggesting that CB was exposed on the surface of the fiber. The presence of CB

in the CNF increased the electrical conductivity of the ink solution during electrospinning due to the properties of the carbon material; this affected the end product of the fiber which was observed to have a thinner CNF diameter with the added CB [28]. However, at the CB/PAN ratio of 0.5, the fiber structures were significantly affected by the CB contents for both Pd/KECNF and Pd/VECNF.

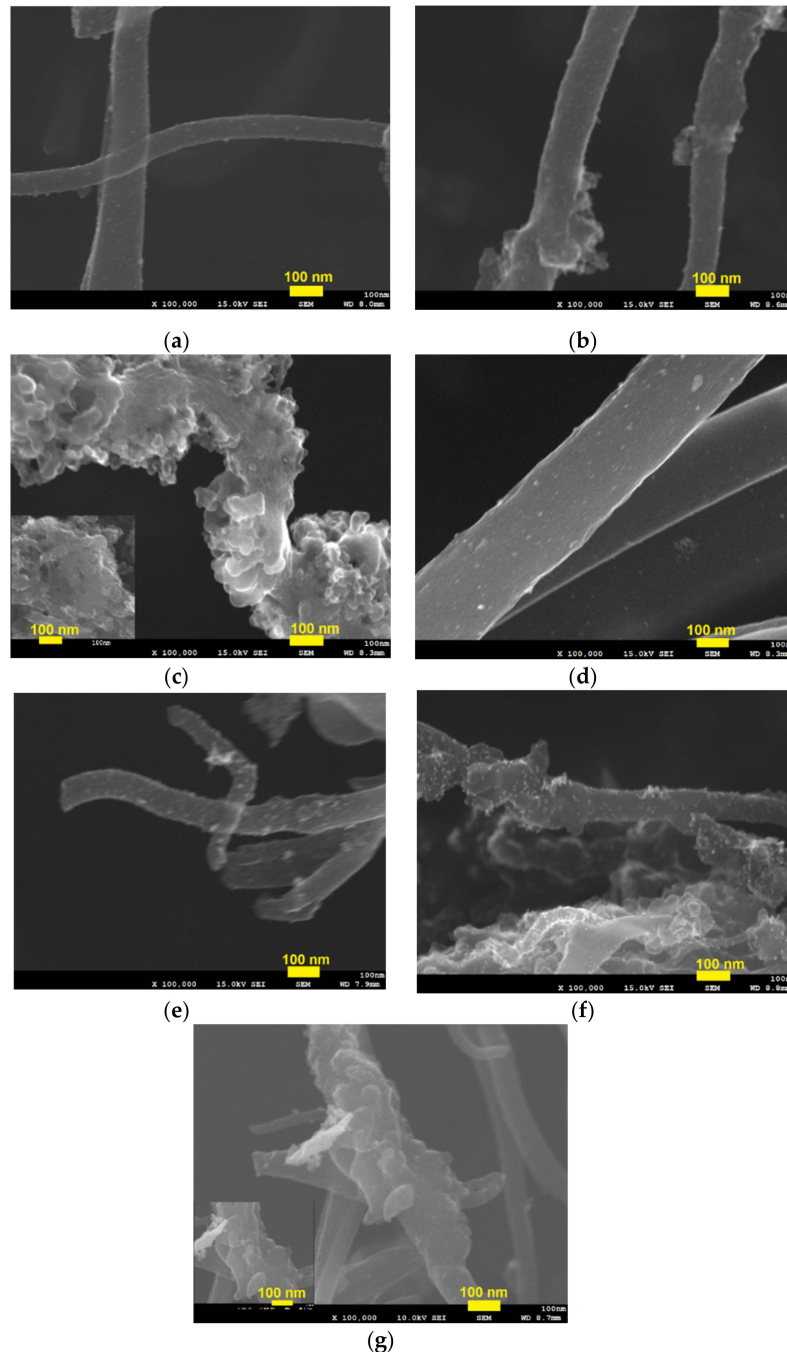


Figure 2. Field emission scanning electron microscope (FESEM) images of (a) Pd/Vulcan-embedded carbon nanofiber (VECNF) [0.125], (b) Pd/VECNF [0.25], (c) Pd/VECNF [0.50], (d) Pd/carbon nanofiber (CNF), (e) Pd/ Ketjen-embedded carbon nanofiber (KECNF) [0.125], (f) Pd/KECNF [0.25], (g) Pd/KECNF [0.50].

Table 3 summarizes the BET surface area, pore volume, and Pd crystallite size of Pd/VECNF and Pd/KECNF for the different weight ratios of CB. As Table 3 shows, the crystallite sizes of Pd were larger than those of Pd/Cs. The influence of the crystallite size in this study was negligible, ranging

between 13.4 and 17.0 nm, because the effect of particles larger than 10 nm is not significant on the FAOR activity [29]. The BET surface area of Pd/KECNF was higher than that of Pd/VECNF. This is due to the Vulcan having a lower BET surface area than Ketjen. It was found that the BET surface areas of the VECNFs were lower than those of Pd/CNF, which contains no CB in the CNF, because the BET surface area of Vulcan ($226 \text{ m}^2 \text{ g}^{-1}$) was lower than that of the CNF ($650 \text{ m}^2 \text{ g}^{-1}$). Considering this fact, the BET surface area should decrease with the increasing Vulcan content; however, Pd/VECNF [0.25] showed a slightly higher BET surface area than Pd/VECNF [0.125]. On the other hand, Pd/KECNF [0.25] and Pd/KECNF [0.50] exhibited higher BET surface areas than Pd/CNF, whereas Pd/KECNF [0.125] exhibited a lower BET surface area. This is because the BET surface area of Ketjen ($849 \text{ m}^2 \text{ g}^{-1}$) is higher than that of CNF. However, there is a slight difference in the BET surface area between Pd/KECNF [0.25] and Pd/KECNF [0.50]. This is because only a small amount of Ketjen was exposed on the surface due to the existence of numerous beads.

Table 3. Summary of the BET surface areas, pore volumes, and Pd crystallite sizes for VECNF and KECNF catalysts with different CB/ polyacrylonitrile (PAN) ratios.

| Catalyst | Surface Area ($\text{m}^2 \text{ g}^{-1}$) | Pore Volume ($\text{cm}^3 \text{ g}^{-1}$) | Pd Crystallite Size (nm) |
|------------------|--|--|--------------------------|
| Pd/CNF | 544 | 0.28 | 17.0 |
| Pd/VECNF [0.125] | 321 | 0.20 | 15.8 |
| Pd/VECNF [0.25] | 391 | 0.44 | 15.8 |
| Pd/VECNF [0.50] | 250 | 0.43 | 13.4 |
| Pd/KECNF [0.125] | 405 | 0.25 | 13.7 |
| Pd/KECNF [0.25] | 573 | 0.43 | 14.1 |
| Pd/KECNF [0.50] | 558 | 0.49 | 15.9 |

Referring to the pore distributions shown in Figure 3 and Figure S4, and the nitrogen adsorption and desorption isotherms shown in Figure S5, the mesopore volume of the Pd/KECNFs increased compared to the Pd/CNF irrespective of the weight ratio of CB/PAN, although the volumes of the mesopores and micropores were smaller than those of Pd/C_k-all. Considering the fact that the mesopore volume of the Pd/KECNF [0.50] was high, it is assumed that a large part of the surface of CNF was covered by the Ketjen, similar to the case of Pd/VECNF [0.50]. In the case of Ketjen, the influence of the weight ratio of the Ketjen/PAN on the BET surface area and the crystallite size of Pd was insignificant; however, it is suggested that the ratio of the Ketjen at the CNF surface would affect the FAOR activity. On the basis of these results and the FESEM observations, it was suggested that the surface of Pd/VECNF [0.50] was almost covered with the Vulcan, which may restrict the utilization of the Pd catalyst due to agglomeration of the fiber structure. Few pores with sizes above 20 nm were observed in the Pd/VECNF [0.125], similar to the case of Pd/CNF. This result indicated that a large amount of CB existed inside the fibers, in agreement with the FESEM observations.

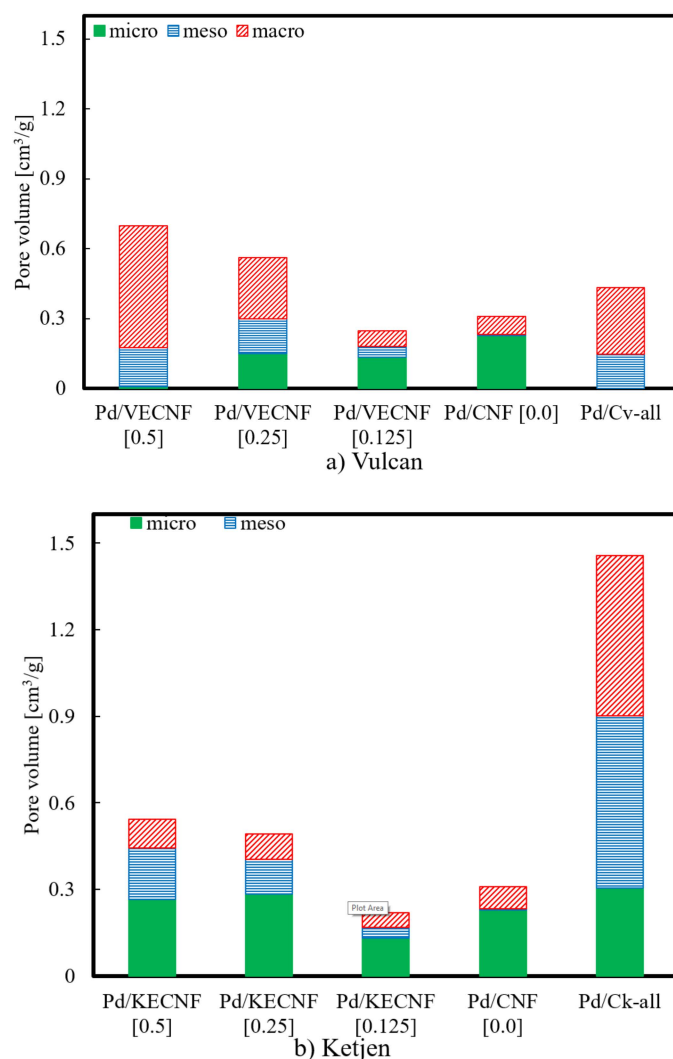


Figure 3. Effect of CB/PAN ratio of VECNF and KECNF on pore distribution for (a) Vulcan and (b) Ketjen.

3.4. Formic Acid Oxidation Reaction on Carbon Black Embedded in Carbon Nanofibers

Figure S6 shows the effect of the CB content in the CNF on the FAOR activity during an anodic scan. Pd/CNF exhibited a relatively low FAOR activity due to the excessive development of micropores, which is similar to that reported by other researchers (around $105\text{--}410\text{ mA mg}_{\text{Pd}}^{-1}$) [13,30–33]. On the other hand, the FAOR activity increased after embedding the CB into the CNFs, and there was a significant difference in the FAOR activity depending on the CB/PAN ratio. The CB/PAN ratio of 0.25 for both Pd/VECNF and Pd/KECNF showed the highest FAOR activities of $1477\text{ mA mg}_{\text{Pd}}^{-1}$ and $2022\text{ mA mg}_{\text{Pd}}^{-1}$, respectively. These values are higher than those obtained for the unembedded CBs that were carbonized and steam activated: Pd/C_v-all and Pd/C_k-all. Essentially, the FAOR activity significantly increased in the case of Pd/KECNF. The maximum catalytic activity obtained in Figure S6 and ECSA for Pd/VECNF and Pd/KECNF are summarized in Table 4. ECSA for Pd/VECNF at the various CB/PAN ratios only have a small deviation despite the mass activity. Hence, the mass activity is not only influenced by the ECSA but may be caused by the metal–support interaction. The metal–support interaction and chemical state influence were investigated by XPS measurements in the next section. Even though the mass activity for the Pd/VECNF and Pd/C_v only have a small difference, the ECSA value of Pd/VECNF being higher than that of Pd/C_v may due to the change in the surface area of the embedded CNF. ECSA for Pd/KECNF was enhanced with the mass activity of the catalyst, reaching the highest ECSA value at $56.9\text{ m}^2\text{ g}_{\text{Pd}}^{-1}$ for Pd/KECNF[0.25] which is comparable to

the Pd/Graphene, which obtained $56.0 \text{ m}^2 \text{ g}_{\text{Pd}}^{-1}$ as reported by Zhang et al. [27]. Generally, Pd/KECNF shows a higher ECSA value compared to Pd/C_k whether heat-treated nor untreated. Note that this was not due to the difference in the Pd particle size, because the Pd crystallite size was much larger in Pd/VECNF and Pd/KECNF than in Pd/CB, with a range 13.4–17.0 nm, as shown in Table 1. The larger Pd particles naturally reduce the electrochemical surface area, which causes a lower FAOR activity. The larger particle size of Pd may affect the FAOR activity; however, this is not a decisive factor for a high electro-catalytic activity especially in this study. The effect of particle size on FAOR in this study is less important because the particle size is larger than 10 nm for Pd/KECNF and Pd/VECNF [29]. Moreover, there was a higher ECSA value in Pd/KECNF and Pd/VECNF compared to Pd/CB despite the smaller crystallite size of Pd/CB, which was caused by the Pd particles in Pd/CB being hidden in the macropore of Pd/CB, which was attributed to low Pd utilization. Pd/KECNF and Pd/VECNF have a higher amount of smaller pores, especially micropore and mesopore along the fiber structure, which provide higher utilization of Pd, hence the enhanced ECSA value. The high FAOR activities of Pd/VECNF and Pd/KECNF must be due to the positive effect of the heat-treated CB, as a result, for example, of the appearance of hydrogen spillover as already mentioned; this does not involve the splitting of the agglomerates or aggregates of the CB due to the protection by the CNF. Since the pore structure of Ketjen was more influenced by heat treatment than that of Vulcan due to its hollow structure (as previously mentioned), a significant increase in the FAOR activity was observed in the case of Pd/KECNF due to the positive effect of the heat treatment of Ketjen [0.25]. Regarding the CB/PAN ratio, there was an optimum weight ratio for both types of CB. The fact that the FAOR activity of Pd/CNF was low suggests that the amount of CB exposed on the CNF surface was also low; this was confirmed by the pore distributions shown in Figure 3 and resulted in the lower supporting effect of the CB when the CB ratio was low, as can be seen in the case of the CB/PAN ratio of 0.125. On the other hand, the CNF structure was damaged at high CB/PAN ratios such as 0.50 because the CNF surface was almost entirely covered by the CB. For these reasons, the optimum CB/PAN ratio was 0.25 under these conditions of heat treatment. If the conditions of the heat treatment, such as the carbonization/steam activation temperature and dew point of the steam, vary, the amount of CB exposed at the CNF surface and the extent of alteration of the carbon microstructure may be significantly different. Maximum mass activity at the peak potential of the CV measurement is crucial to determine the activity of the promising catalyst in actual fuel cell applications [34].

Table 4. Summary of catalytic activity and electrochemical active surface area of Pd/VECNF and Pd/KECNF for various CB/PAN ratios.

| Catalyst | Mass Activity at Ep, ip-FAOR ($\text{mA mg}_{\text{Pd}}^{-1}$) | Peak Potential, Ep (V vs. NHE) | Electrochemical Active Surface Area ($\text{m}^2 \text{ g}_{\text{Pd}}^{-1}$) |
|------------------|---|-----------------------------------|--|
| Pd/VECNF [0.5] | 486 | 0.52 | 38.5 |
| Pd/VECNF [0.25] | 1477 | 0.56 | 35.5 |
| Pd/VECNF [0.125] | 481 | 0.38 | 39.9 |
| Pd/KECNF [0.5] | 945 | 0.52 | 35.8 |
| Pd/KECNF [0.25] | 2022 | 0.62 | 56.9 |
| Pd/KECNF [0.125] | 1096 | 0.60 | 25.1 |
| Pd/CNF [0.0] | 398 | 0.50 | 20.1 |

Modification of the catalyst support material possibly contributes to the activity of the catalyst due to its bonding to the catalyst metal. This metal–support interaction modifies both the electronic and geometric properties of the catalyst support, which influences the activity of the catalytic sites on the metal surface and enhances the presence of active sites [17]. In this study, XPS was used to determine the active sites of Pd, thus providing crucial information about the metal–support interaction by observing the electronic modifications of the metal which contribute to the improvement of the FAOR activity. Figure 4 shows the wide scan XPS results for the chemical element contained in the supported Pd catalysts. Figure 5 shows the surface state of Pd3d, which shows the surface composition

and oxidation state of the metal on the Pd/CNF, Pd/KECNF, and Pd/VECNF catalysts with different mass ratios of Ketjen and Vulcan carbon black to PAN, and indicates a possible electronic interaction [25]. Table 5 shows that the metal state of CB/PAN [0.25] for both Pd/KECNF and Pd/VECNF has the highest relative intensity of Pd metal (Pd^0) compared to CB/PAN [0.125] and [0.5] which support the fact that CB/PAN [0.25] was the optimum CB/PAN ratio to increase the metal–support interaction. Moreover, the presence of PdO_2 (Pd^{4+}), which is a highly active catalyst due to its instability, enhances the FAOR activity [35]. Even though Pd/VECNF [0.25] has a higher Pd metal content compared to Pd/KECNF [0.25], the high relative intensity of Pd^{4+} in Pd/KECNF [0.25] contributed to the higher FAOR activity. The optimum ratio of CB/PAN gives a great improvement in the Pd metal state, which improves the interaction between the carbon and Pd. The addition of CB embedded into the CNF improves the active sites of Pd/KECNF and Pd/VECNF in a similar way to the presence of PdO (Pd^{2+}) and PdO_2 ; this is not the case for the Pd/VECNF 0.5 in which the highly oxidized Pd (Pd^{4+}) was absent. This state may be due to the concentration of carbon material for Vulcan/PAN at 0.5. At a low ratio of CB/PAN, such as 0.125, the effect of the carbon black was insufficient to shift the binding energy of $\text{Pd}3d_{(5/2)}$; however, only Pd^{2+} and Pd^{4+} for Pd/KECNF caused a positive shift compared to Pd/VECNF, for CB/PAN at ratios 0.125 and 0.25. The shift in the binding energy indicates a stronger interaction between the Pd particles and the carbon support, therefore, the role of particle size (as demonstrated in the XRD data) without a particular trend can be discounted [12]. The low interaction of the metal support will increase the tendency for oxidation [36]. The FAOR activity is affected by the formation of the new active sites due to interaction from the Pd and carbon [12,37], as can be observed by the addition of carbon material to the support affecting the FAOR activity, no matter how the particle size changed. In this study, the modification of the electronic and catalytic properties is the key factor for the improvement of the FAOR activity, which is in agreement with previous research [12,25,38].

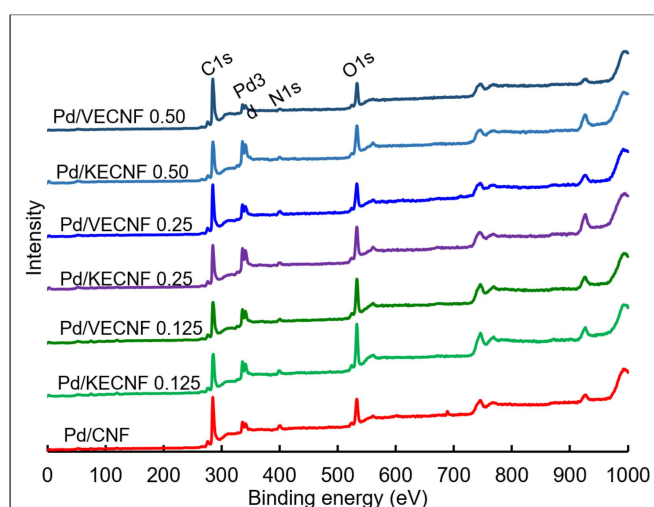


Figure 4. X-ray photoelectron spectroscopy (XPS) spectra for the wide scan of Pd supported CB-embedded CNF.

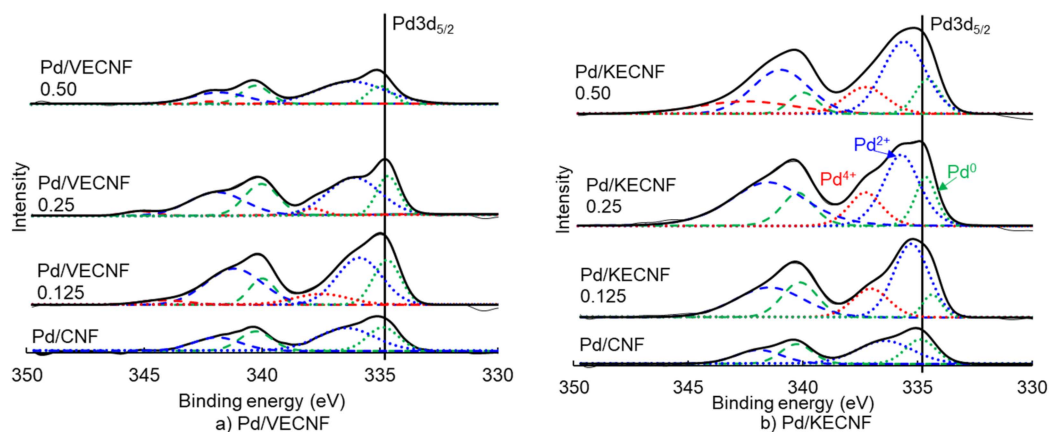


Figure 5. Narrow scan of the Pd3d spectrum for different ratios of (a) Pd/VECNF and (b) Pd/KECNF, compared to Pd/CNF.

Table 5. Binding energy Pd3d_(5/2) and relative intensities of surface Pd species from the Pd3d XPS of Pd/CB-embedded carbon nanofiber.

| Catalyst Samples | Pd Surface Species | Binding Energy (eV) | Relative Intensity |
|------------------|--------------------|---------------------|--------------------|
| Pd/CNF | Pd ⁰ | 334.88 | 0.51 |
| | Pd ²⁺ | 336.44 | 0.49 |
| | Pd ⁴⁺ | | 0.00 |
| Pd/KECNF 0.125 | Pd ⁰ | 334.37 | 0.18 |
| | Pd ²⁺ | 335.28 | 0.59 |
| | Pd ⁴⁺ | 337.05 | 0.23 |
| Pd/KECNF 0.25 | Pd ⁰ | 334.65 | 0.32 |
| | Pd ²⁺ | 335.71 | 0.46 |
| | Pd ⁴⁺ | 337.27 | 0.22 |
| Pd/KECNF 0.5 | Pd ⁰ | 334.56 | 0.26 |
| | Pd ²⁺ | 335.59 | 0.54 |
| | Pd ⁴⁺ | 337.28 | 0.20 |
| Pd/VECNF 0.125 | Pd ⁰ | 334.72 | 0.44 |
| | Pd ²⁺ | 335.89 | 0.46 |
| | Pd ⁴⁺ | 337.51 | 0.10 |
| Pd/VECNF 0.25 | Pd ⁰ | 334.68 | 0.47 |
| | Pd ²⁺ | 336.13 | 0.45 |
| | Pd ⁴⁺ | 337.86 | 0.08 |
| Pd/VECNF0.5 | Pd ⁰ | 335.01 | 0.44 |
| | Pd ²⁺ | 336.24 | 0.56 |
| | Pd ⁴⁺ | | 0.00 |

4. Conclusions

The effects of the heat treatment of the CBs, Vulcan XC-72 and Ketjen black, on their morphologies, pore volume distributions, and FAOR activity were investigated with the aim of clarifying the high FAOR activity observed for Vulcan embedded into CNFs, as reported in a previous study [13]. Moreover, the different weight ratios of Vulcan XC-72 and Ketjen black embedded in the CNF were also synthesized to clarify the factors affecting the FAOR activity of the CB embedded in the CNF. Pd catalysts supported by Vulcan exhibited a higher FAOR activity after steam activation or carbonization. On the other hand, Pd supported by Vulcan after both carbonization and steam activation exhibited a lower FAOR activity compared to only carbonization or steam activation. Moreover, Pd supported by Ketjen showed no improvement in the FAOR activity, irrespective of the kind of heat treatment.

On the basis of an analysis of the pore volume distributions, it was suggested that excessive CB heat treatment destroyed the carbon structure and/or pore growth, and Ketjen was more prone to structural damage due to its hollow and porous structure. On the basis of these results, it was found that the appropriate heat treatment of the CB was effective for enhancing the FAOR activity due to the metal–support interactions, but excessive heat treatment caused a decrease in the FAOR activity due to the destruction of the CB microstructure, especially for Pd/C_k. The effect of the CB on the CNF ratio was also investigated using Vulcan and Ketjen black. Pd/VECNF [0.25] and Pd/KECNF [0.25] showed a higher FAOR activity compared to the pure CBs that were only heat-treated. In particular, Pd/KECNF showed the highest FAOR catalytic activity and ECSA value among all the catalysts. These results were attributed to the appearance of the metal–support effect after the appropriate heat treatment of the CB and protection of the CB structure by the CNF. Moreover, the CB/PAN weight ratio which gave rise to the optimal catalytic activity was 0.25, because the amount of CB exposed on the surface of the CNF was the most appropriate. The metal–support interaction of the supported catalyst was confirmed by the XPS data, which showed that a shift in the binding energy promotes COOH oxidation.

This study successfully showed that by embedding CB into the CNFs to form the support for the Pd catalysts (both Pd/VECNF and Pd/KECNF), the mass activity of the catalyst was improved compared to Pd/CNF and the conventional Pd/C. At the CB/PAN ratio of 0.25, and especially in the case of Pd/KECNF, an excellent FAOR activity was obtained. On the basis of these results, KECNF is considered to be a promising Pd support for DFAFC anodes.

Supplementary Materials: The following are available online at <http://www.mdpi.com/2076-3417/9/24/5542/s1>, Figure S1: Pore size distribution for Pd/C_v and Pd/C_k with various heat treatments, Figure S2: Nitrogen adsorption and desorption isotherms for (a) Pd/C_v and (b) Pd/C_k with various heat treatments, Figure S3: Cyclic voltammetry of (a) Pd/C_v and (b) Pd/C_k with various heat treatments, Figure S4: Pore size distribution for Pd/KECNF and Pd/VECNF for various CB/PAN ratios, Figure S5: Nitrogen adsorption and desorption isotherms for (a) Pd/VECNF and (b) Pd/KECNF for various CB/PAN ratios, Figure S6: Cyclic voltammetry of (a) Pd/VECNF and (b) Pd/KECNF for various CB/PAN ratios.

Author Contributions: Writing—original draft preparation, N.M.A.; writing—review and editing, T.T.; supervision, T.T., Y.O., A.K.

Funding: This study was supported by JST Network of PRESTO and JSPS KAKENHI 18H01774.

Conflicts of Interest: The authors declare no conflict of interest.

References

1. Rees, N.V.; Compton, R.G. Sustainable energy: A review of formic acid electrochemical fuel cells. *J. Solid State Electrochem.* **2011**, *15*, 2095–2100. [[CrossRef](#)]
2. Hong, P.; Liao, S.; Zeng, J.; Huang, X. Design, fabrication and performance evaluation of a miniature air breathing direct formic acid fuel cell based on printed circuit board technology. *J. Power Sources* **2010**, *195*, 7332–7337. [[CrossRef](#)]
3. Aslam, N.M.; Masdar, M.S.; Kamarudin, S.K.; Daud, W.R.W. Overview on Direct Formic Acid Fuel Cells (DFAFCs) as an Energy Sources. *APCBEE Procedia* **2012**, *3*, 33–39. [[CrossRef](#)]
4. Hong, P.; Luo, F.; Liao, S.; Zeng, J. Effects of Pt/C, Pd/C and PdPt/C anode catalysts on the performance and stability of air breathing direct formic acid fuel cells. *Int. J. Hydrogen Energy* **2011**, *36*, 8518–8524. [[CrossRef](#)]
5. Haan, J.L.; Masel, R.I. The influence of solution pH on rates of an electrocatalytic reaction: Formic acid electrooxidation on platinum and palladium. *Electrochim. Acta* **2009**, *54*, 4073–4078. [[CrossRef](#)]
6. Jayashree, R.; Spendelow, J.; Yeom, J.; Rastogi, C.; Shannon, M.; Kenis, P. Characterization and application of electrodeposited Pt, Pt/Pd, and Pd catalyst structures for direct formic acid micro fuel cells. *Electrochim. Acta* **2005**, *50*, 4674–4682. [[CrossRef](#)]
7. Huang, Y.; Zhou, X.; Liao, J.; Liu, C.; Lu, T.; Xing, W. Preparation of Pd / C catalyst for formic acid oxidation using a novel colloid method. *Electrochem. Commun.* **2008**, *10*, 621–624. [[CrossRef](#)]
8. Bianchini, C.; Shen, P.K. Palladium-based electrocatalysts for alcohol oxidation in half cells and in direct alcohol fuel cells. *Chem. Rev.* **2009**, *109*, 4183–4206. [[CrossRef](#)]

9. Sharma, S.; Pollet, B.G. Support materials for PEMFC and DMFC electrocatalysts—A review. *J. Power Sources* **2012**, *208*, 96–119. [[CrossRef](#)]
10. Yu, X.; Pickup, P.G. Recent advances in direct formic acid fuel cells (DFAFC). *J. Power Sources* **2008**, *182*, 124–132. [[CrossRef](#)]
11. Holade, Y.; Morais, C.; Servat, K.; Napporn, T.W.; Kokoh, K.B. Enhancing the available specific surface area of carbon supports to boost the electroactivity of nanostructured Pt catalysts. *Phys. Chem. Chem. Phys.* **2014**, *16*, 25609–25620. [[CrossRef](#)] [[PubMed](#)]
12. Chang, J.; Li, S.; Feng, L.; Qin, X.; Shao, G. Effect of carbon material on Pd catalyst for formic acid electrooxidation reaction. *J. Power Sources* **2014**, *266*, 481–487. [[CrossRef](#)]
13. Onishi, R.; Tsujiguchi, T.; Osaka, Y.; Kodama, A. High Formic Acid Oxidation Activity and Stability of Pd Catalyst Supported by Nanoparticle-Embedded Carbon Nanofiber. *ECS Trans.* **2015**, *69*, 663–674. [[CrossRef](#)]
14. Ito, Y.; Takeuchi, T.; Tsujiguchi, T.; Abdelkareem, M.A.; Nakagawa, N. Ultrahigh methanol electro-oxidation activity of PtRu nanoparticles prepared on TiO₂-embedded carbon nano fiber support. *J. Power Sources* **2013**, *242*, 280–288. [[CrossRef](#)]
15. Kunitomo, H.; Ishitobi, H.; Nakagawa, N. Optimized CeO₂ content of the carbon nanofiber support of PtRu catalyst for direct methanol fuel cells. *J. Power Sources* **2015**, *297*, 400–407. [[CrossRef](#)]
16. Inoue, H.; Hosoya, K.; Kannari, N.; Ozaki, J. Influence of heat-treatment of Ketjen Black on the oxygen reduction reaction of Pt/C catalysts. *J. Power Sources* **2012**, *220*, 173–179. [[CrossRef](#)]
17. Antolini, E.; Gonzalez, E.R.R. Carbon supports for low-temperature fuel cell catalysts. *Appl. Catal. B Environ.* **2009**, *88*, 1–24. [[CrossRef](#)]
18. Hassan, A.; Carreras, A.; Trincavelli, J.; Ticianelli, E.A. Effect of heat treatment on the activity and stability of carbon supported PtMo alloy electrocatalysts for hydrogen oxidation in proton exchange membrane fuel cells. *J. Power Sources* **2014**, *247*, 712–720. [[CrossRef](#)]
19. Valisi, A.N.; Maiyalagan, T.; Khotseng, L.; Linkov, V.; Pasupathi, S. Effects of Heat Treatment on the Catalytic Activity and Methanol Tolerance of Carbon-Supported Platinum Alloys. *Electrocatalysis* **2012**, *3*, 108–118. [[CrossRef](#)]
20. Zhang, J.; Chen, M.; Li, H.; Li, Y.; Ye, J.; Cao, Z.; Fang, M.; Kuang, Q.; Zheng, J.; Xie, Z. Stable palladium hydride as a superior anode electrocatalyst for direct formic acid fuel cells. *Nano Energy* **2018**, *44*, 127–134. [[CrossRef](#)]
21. Chen, C.-H.; Huang, C.-C. Enhancement of hydrogen spillover onto carbon nanotubes with defect feature. *Microporous Mesoporous Mater.* **2008**, *109*, 549–559. [[CrossRef](#)]
22. Nataraj, S.K.; Yang, K.S.; Aminabhavi, T.M. Polyacrylonitrile-based nanofibers—A state-of-the-art review. *Prog. Polym. Sci.* **2012**, *37*, 487–513. [[CrossRef](#)]
23. Soboleva, T.; Zhao, X.; Malek, K.; Xie, Z.; Navessin, T.; Holdcroft, S. On the micro-, meso-, and macroporous structures of polymer electrolyte membrane fuel cell catalyst layers. *ACS Appl. Mater. Interfaces* **2010**, *2*, 375–384. [[CrossRef](#)]
24. Liang, J.-Z. Effects of heat treatment on electrical conductivity of HDPE/CB composites. *Polym. Test.* **2017**, *62*, 219–224. [[CrossRef](#)]
25. Zhao, X.; Zhu, J.; Liang, L.; Liu, C.; Liao, J.; Xing, W. Enhanced electroactivity of Pd nanocrystals supported on H₃PMo₁₂O₄₀/carbon for formic acid electrooxidation. *J. Power Sources* **2012**, *210*, 392–396. [[CrossRef](#)]
26. Park, Y.-C.; Tokiwa, H.; Kakinuma, K.; Watanabe, M.; Uchida, M. Effects of carbon supports on Pt distribution, ionomer coverage and cathode performance for polymer electrolyte fuel cells. *J. Power Sources* **2016**, *315*, 179–191. [[CrossRef](#)]
27. Zhang, L.Y.; Zhao, Z.L.; Li, C.M. Formic acid-reduced ultrasmall Pd nanocrystals on graphene to provide superior electrocatalytic activity and stability toward formic acid oxidation. *Nano Energy* **2015**, *11*, 71–77. [[CrossRef](#)]
28. Inagaki, M.; Yang, Y.; Kang, F. Carbon nanofibers prepared via electrospinning. *Adv. Mater.* **2012**, *24*, 2547–2566. [[CrossRef](#)]
29. Hu, S.; Che, F.; Khorasani, B.; Jeon, M.; Yoon, C.W.; McEwen, J.-S.; Scudiero, L.; Ha, S. Improving the electrochemical oxidation of formic acid by tuning the electronic properties of Pd-based bimetallic nanoparticles. *Appl. Catal. B Environ.* **2019**, *254*, 685–692. [[CrossRef](#)]

30. Nitze, F.; Mazurkiewicz, M.; Malolepszy, A.; Mikolajczuk, A.; Kdzierzawski, P.; Tai, C.W.; Hu, G.; Kurzydłowski, K.J.; Stobinski, L.; Borodzinski, A.; et al. Synthesis of palladium nanoparticles decorated helical carbon nanofiber as highly active anodic catalyst for direct formic acid fuel cells. *Electrochim. Acta* **2012**, *63*, 323–328. [[CrossRef](#)]
31. Hu, G.; Nitze, F.; Barzegar, H.R.; Sharifi, T.; Mikolajczuk, A.; Tai, C.W.; Borodzinski, A.; Wgberg, T. Palladium nanocrystals supported on helical carbon nanofibers for highly efficient electro-oxidation of formic acid, methanol and ethanol in alkaline electrolytes. *J. Power Sources* **2012**, *209*, 236–242. [[CrossRef](#)]
32. Qin, Y.-H.; Jia, Y.-B.; Jiang, Y.; Niu, D.-F.; Zhang, X.-S.; Zhou, X.-G.; Niu, L.; Yuan, W.-K. Controllable synthesis of carbon nanofiber supported Pd catalyst for formic acid electrooxidation. *Int. J. Hydrogen Energy* **2012**, *37*, 7373–7377. [[CrossRef](#)]
33. Qin, Y.H.; Yang, H.H.; Zhang, X.S.; Zhou, X.G.; Niu, L.; Yuan, W.K. Synthesis of highly dispersed and active palladium/carbon nanofiber catalyst for formic acid electrooxidation. *J. Power Sources* **2011**, *196*, 4609–4612. [[CrossRef](#)]
34. Zhang, X.J.; Zhang, J.M.; Zhang, P.Y.; Li, Y.; Xiang, S.; Tang, H.G.; Fan, Y.J. Highly active carbon nanotube-supported Ru@Pd core-shell nanostructure as an efficient electrocatalyst toward ethanol and formic acid oxidation. *Mol. Catal.* **2017**, *436*, 138–144. [[CrossRef](#)]
35. Kibis, L.S.; Stadnichenko, A.I.; Koscheev, S.V.; Zaikovskii, V.I.; Boronin, A.I. Highly oxidized palladium nanoparticles comprising Pd 4+ species: Spectroscopic and structural aspects, thermal stability, and reactivity. *J. Phys. Chem. C* **2012**, *116*, 19342–19348. [[CrossRef](#)]
36. Bueres, R.F.; Asedegbega-Nieto, E.; Díaz, E.; Ordóñez, S.; Díez, F.V. Preparation of carbon nanofibres supported palladium catalysts for hydrodechlorination reactions. *Catal. Commun.* **2008**, *9*, 2080–2084. [[CrossRef](#)]
37. Zheng, J.-S.; Wang, X.-Z.; Fu, R.; Yang, D.-J.; Li, P.; Lv, H.; Ma, J.-X. Microstructure effect of carbon nanofibers on Pt/CNFs electrocatalyst for oxygen reduction. *Int. J. Hydrogen Energy* **2012**, *37*, 4639–4647. [[CrossRef](#)]
38. Zhou, W.; Lee, J.Y. Particle size effects in Pd-catalyzed electrooxidation of formic acid. *J. Phys. Chem. C* **2008**, *112*, 3789–3793. [[CrossRef](#)]



© 2019 by the authors. Licensee MDPI, Basel, Switzerland. This article is an open access article distributed under the terms and conditions of the Creative Commons Attribution (CC BY) license (<http://creativecommons.org/licenses/by/4.0/>).